




Robust edge states in magnetic soliton racetrackZ.-X. Li , Zhenyu Wang , Yunshan Cao, H. W. Zhang, and Peng Yan **School of Electronic Science and Engineering and State Key Laboratory of Electronic Thin Films and Integrated Devices, University of Electronic Science and Technology of China, Chengdu 610054, China*

(Received 4 October 2020; revised 25 January 2021; accepted 17 February 2021; published 25 February 2021)

Precise positioning of magnetic solitons requires controllable artificial pinning, while the accurate determination of the pinning profile remains a challenge. Here, we propose a topological solution to this problem. Taking the domain wall (DW) as a representative example, we study the collective dynamics of interacting DWs in a magnetic racetrack with pinning sites of alternate distances. By mapping the governing equations of DW motion to the Su-Schrieffer-Heeger model and evaluating the quantized Zak phase, we predict two topologically distinct phases in the racetrack. A robust edge state emerges at either one or both ends depending on the parity of the DW number and the ratio of alternating intersite lengths. We show that the in-gap DW oscillation frequency has a fixed value which depends only on the geometrical shape of the pinning notch, and is insensitive to device imperfections and inhomogeneities. The spring coefficient of the pinning potential can be quantified as the square of the robust DW frequency multiplied by its constant mass. Our findings pave the way to determining the pinning potential with high accuracy for generic magnetic solitons and suggest as well that the magnetic soliton-based racetrack is a unique playground to study topological phase transitions.

DOI: [10.1103/PhysRevB.103.054438](https://doi.org/10.1103/PhysRevB.103.054438)**I. INTRODUCTION**

Magnetic solitons like the vortex [1,2], bubble [3,4], skyrmion [5,6], and domain wall (DW) [7–9] have attracted tremendous recent attention owing to their fundamental nature and potential applications in memories, sensors, logic gates, and neuromorphic computing hardware [10–24]. To achieve reliable control of the soliton position in spintronic devices, external pinnings are often introduced by artificial notches [25–30], protrusions [31–35], kinks [36], etc. It has been shown that the shape and strength of the pinning potential can strongly affect the soliton dynamics [37]. For instance, a critical current must be overcome to depin the DW [38,39]. The depinning approach was adopted as well to quantify the spin-transfer torque (STT) non-adiabaticity β [40,41], an important parameter for current-induced magnetization dynamics while its value is still highly controversial in different experiments [40–46]. One reason is the lack of reliable determination of the pinning potential, because the extrinsic pinning is often mixed up with the intrinsic ones originating from materials defects and randomness [47,48], leading to a seemingly insuperable difficulty to distinguish the two contributions.

Topology theory can predict global properties of a physical system, regardless of its details. One of the most outstanding examples is the quantum Hall effect [49], which defines a resistance that depends only on fundamental physical constants due to the robust in-gap edge states, making possible an accurate definition of the ohm. It thus motivates us to pursue a topological method for the realization of the standardized

magnetic-soliton frequency. Topological phases have been studied for spin waves [50–54] and magnetic vortices [55–59].

In this work, we choose the DW as the representative example of magnetic solitons and investigate theoretically the collective dynamics of interacting DWs that are locally pinned by notches in a magnetic racetrack [see Fig. 1(a)]. Without loss of generality, we consider the Néel-type DW in the setup. The governing equation of DW motion is mapped to the Su-Schrieffer-Heeger (SSH) model that allows a topological description. By evaluating the quantized Zak phase, we predict two topologically distinct phases in the racetrack. The bulk-boundary correspondence dictates a robust DW oscillation at the edges. We show that the in-gap DW oscillating frequency manifests a constant value which depends only on the geometrical shape of the pinning notch, and is insensitive to the material imperfection and inhomogeneity. The spring coefficient of the pinning potential then can be accurately quantified as the square of the robust DW frequency multiplied by its constant mass. Full micromagnetic simulations are performed to verify our theoretical predictions with a great agreement. Our results offer the standard of the soliton oscillation frequency and suggest that the magnetic soliton racetrack is a unique playground to study the fundamental topological phase and phase transition, in addition to its practical application in information technology.

The paper is organized as follows. In Sec. II, we present the theoretical model for collective DW motions in a magnetic racetrack with periodic pinning sites. Section III A gives the analytical derivation of the topological phases in the DW racetrack. Micromagnetic simulations are performed in Sec. III B to verify analytical results. Our discussion and conclusion are given in Sec. IV.

*Corresponding author: yan@uestc.edu.cn

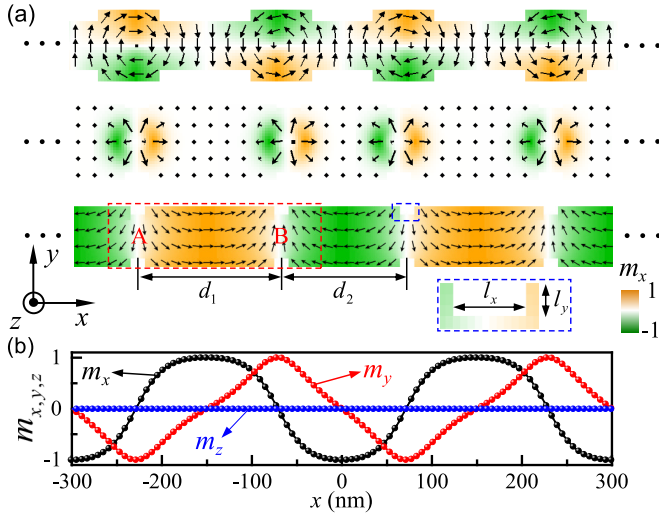


FIG. 1. (a) Illustration of the vortex, skyrmion, and DW racetrack with periodic pinnings. The micromagnetic structure of Néel-type DWs pinned by cuboid notches with $l_x = 20$ nm, $l_y = 9$ nm, and $l_z = 5$ nm is plotted, with the unit cell containing two DWs at sites A and B. d_1 and d_2 are the intracellular and intercellular distances between notches, respectively. (b) The components of normalized magnetization along the center of DW racetrack with $d_1 = 160$ nm and $d_2 = 140$ nm.

II. THEORETICAL MODEL

We start with the Landau-Lifshitz-Gilbert equation that governs the magnetization dynamics [60,61]:

$$\frac{\partial \mathbf{m}}{\partial t} = -\gamma \mathbf{m} \times \mathbf{H}_{\text{eff}} + \alpha \mathbf{m} \times \frac{\partial \mathbf{m}}{\partial t} + \mathbf{\Gamma}_{\text{st}}, \quad (1)$$

where $\mathbf{m} = \mathbf{M}/M_s$ is the unit magnetization vector with the saturated magnetization M_s , γ is the gyromagnetic ratio, and α is the Gilbert damping constant. The effective field \mathbf{H}_{eff} comprises the external field, the exchange field, the magnetic anisotropic field, and the dipolar field. $\mathbf{\Gamma}_{\text{st}}$ is the torque due to the spin-transfer or spin-orbit effects. For the case of STT, $\mathbf{\Gamma}_{\text{st}} = b_J(\hat{J} \cdot \nabla)\mathbf{m} - \beta b_J \mathbf{m} \times (\hat{J} \cdot \nabla)\mathbf{m}$ with $b_J = JPg\mu_B/2|e|M_s$ and \hat{J} being the flow direction of the spin-polarized current. Here J is the charge current density, P is the spin polarization, g is the g factor, μ_B is the Bohr magneton, and e is the (negative) electron charge.

The collective-coordinate or $\{q, \phi\}$ method provides a simple yet accurate description of the motion of complex DWs [see Fig. 1(b)] [62,63]:

$$\begin{aligned} (1 + \alpha^2) \frac{dq_j}{dt} &= \gamma \alpha H_{\text{pin},j} \Delta_j + \frac{1}{2} \gamma (N_z - N_y) \Delta_j M_s \sin 2\phi_j, \\ (1 + \alpha^2) \frac{d\phi_j}{dt} &= \gamma H_{\text{pin},j} - \frac{1}{2} \gamma \alpha (N_z - N_y) M_s \sin 2\phi_j, \end{aligned} \quad (2)$$

where the collective coordinates q_j and ϕ_j are the position and tilt angle of the j th DW, respectively, $H_{\text{pin},j}$ includes the pinning field from both the notch and the DW-DW interaction, N_y and N_z are the demagnetizing factors along the y and z axes of the nanostrip, respectively, and $\Delta_j = \sqrt{2A/[2K_u + \mu_0 M_s^2[(N_y - N_x) + (N_z - N_y)\sin^2 \phi_j]]}$

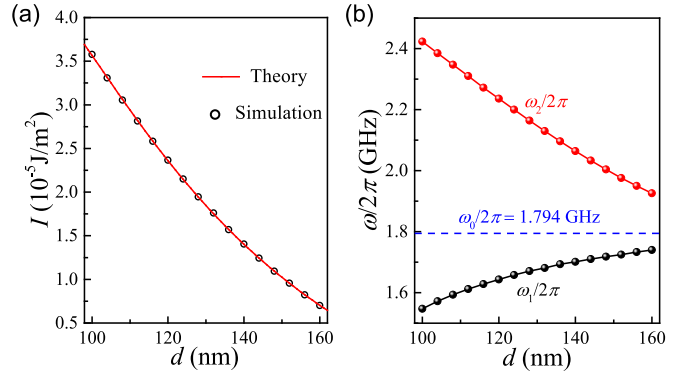


FIG. 2. (a) Dependence of the coupling strength I on d . Black circles denote simulation results and red solid line represents the analytical formula. (b) The two eigenfrequencies of a DW-DW pair varying with d .

represents the DW width with A the exchange stiffness, K_u the magnetocrystalline anisotropy constant, and μ_0 being the vacuum permeability. Since we are interested in the genuine oscillation of the DW near the pinning notch, we have assumed that the spin torque is absent in Eq. (2), while it can be straightforwardly included and analyzed (see below).

From the energy point of view, $H_{\text{pin},j}$ can be expressed as the spatial derivative of the total potential:

$$H_{\text{pin},j} = -\frac{1}{2\mu_0 M_s L_y L_z} \frac{\partial U}{\partial q_j}, \quad (3)$$

where L_y and L_z are the width and thickness of the nanostrip, respectively, and U is the total energy of the system: $U = \sum_j \mathcal{K} q_j^2/2 + \sum_{j \neq k} I(d_{jk}) q_j q_k/2$. Here \mathcal{K} is the spring constant determined by the shape of the notch and $I(d_{jk})$ is the coupling constant depending on the distance d_{jk} between DWs. Generally, the DW-DW interaction can be divided into three parts: the monopole-monopole ($\propto 1/d_{jk}$), the exchange ($\propto 1/d_{jk}^2$), and the dipole-dipole ($\propto 1/d_{jk}^3$) [64]. The explicit form of $I(d)$ can be obtained from micromagnetic simulations in a self-consistent manner. Considering a small ϕ and neglecting the dissipation terms, we arrive at the linear form of Eq. (2):

$$\mathcal{M} \frac{d^2 q_j}{dt^2} + \mathcal{K} q_j + \sum_{k \in \langle j \rangle} I(d_{jk}) q_k = 0, \quad (4)$$

where the $\mathcal{M} = 2\mu_0 L_y L_z / \gamma^2 (N_z - N_y) \Delta$ is the effective mass of a single DW with $\Delta = \sqrt{2A/[2K_u + \mu_0 M_s^2 (N_y - N_x)]}$ and $\langle j \rangle$ is the set of the nearest neighbors of j . Here, $I(d_{jk}) = I_1$ (I_2) when j and k share an intracellular (intercellular) connection with $I_{1,2} = I(d_{1,2})$ (d_1 and d_2 are the alternating intersite lengths). To obtain the analytical formula of $I(d)$, we simulate the dynamic of a DW-DW pair separated by an arbitrary distance (see Appendix A for details). Symbols in Fig. 2(a) are numerical results and the solid curve is theoretical formula $I(d) = c_1/d + c_2/d^2 + c_3/d^3$, with $c_1 = -9.2635 \times 10^{-12}$ J m $^{-1}$, $c_2 = 2.294 \times 10^{-18}$ J, and $c_3 = -1.0111 \times 10^{-25}$ J m. Figure 2(b) plots the d dependence of the out-of-phase and in-phase DW-oscillation frequencies, that is, ω_1 and ω_2 , respectively, in the simple two-DW system. It shows that ω_1

increases while ω_2 decreases for an increasing d . One naturally expects that $\omega_1 = \omega_2 = \omega_0$ when $d \rightarrow \infty$, with $\omega_0 = \sqrt{\mathcal{K}/M}$ corresponding to the oscillation frequency of an isolated DW. By measuring ω_0 in experiments, one can determine the pinning-potential stiffness \mathcal{K} . This approach, however, suffers from an issue that the dynamics of a single DW can be easily modified by structure defects and material randomness, and it thus cannot precisely determine the genuine profile of the pinning potential. Below, we propose a topological method to overcome this problem.

III. RESULTS

A. Topological phase in DW racetrack

We consider a one-dimensional DW lattice, as plotted in Fig. 1(a), where the dashed red rectangle represents the unit cell and the basis vector is $\mathbf{a} = a\hat{x}$ with $a = d_1 + d_2$. The band structure of the collective DW oscillations can be computed by a plane wave expansion $q_j = q_j \exp[i(\omega t + nka)]$, where $j = A, B$ for different sublattices, n is an integer, and k is the wave vector. Substituting the Fourier transformation into Eq. (4), we obtain the Hamiltonian expressed in the momentum space as

$$\mathcal{H} = \begin{pmatrix} \mathcal{K} & I_1 + I_2 e^{-ika} \\ I_1 + I_2 e^{ika} & \mathcal{K} \end{pmatrix} \quad (5)$$

$$= [I_1 + I_2 \cos(ka)]\sigma_x + I_2 \sin(ka)\sigma_y + \mathcal{K}\sigma_0,$$

where $\sigma_x = \begin{pmatrix} 0 & 1 \\ 1 & 0 \end{pmatrix}$, $\sigma_y = \begin{pmatrix} 0 & -i \\ i & 0 \end{pmatrix}$, and $\sigma_0 = \begin{pmatrix} 1 & 0 \\ 0 & 1 \end{pmatrix}$ are the Pauli matrices. Comparing Eq. (5) with the Hamiltonian of the SSH model [65,66], one can see that our model contains an extra constant diagonal term $\mathcal{K}\sigma_0$, which represents the on site energy and is independent of the wave vector. It only shifts the position of the band center (zero-energy point) while the topological feature of the system remains identical by setting it to be zero. I_1 and I_2 in (5) represent the alternating hopping amplitudes between the ‘‘A’’ and ‘‘B’’ sites of the diatomic lattice. We therefore conclude that our Hamiltonian is mapped to the SSH model.

Solving (5) gives the dispersion relation:

$$\omega_{\pm}(k) = \sqrt{\frac{\mathcal{K} \pm \sqrt{I_1^2 + I_2^2 + 2I_1 I_2 \cos ka}}{M}}, \quad (6)$$

where $+$ ($-$) represents the optical (acoustic) branch. The bulk band structures for different geometric parameters are plotted in Fig. 3(a), where d_2 is fixed to 140 nm if not stated otherwise and magnetic parameters of Ni are adopted. For $d_1 = d_2$, the two bands merge together [black curve in Fig. 3(a)], while a gap opens at $k = \pi/a$ when $d_1 \neq d_2$ [red and blue curves in Fig. 3(a)], leading to an insulating phase. To judge whether these insulating phases are topological, we consider the Zak phase [67], a topological invariant that is evaluated by integrating the Berry connection over the first Brillouin zone:

$$\mathbb{Z} = i \int_0^{2\pi/a} \Psi^\dagger(k) \nabla_k \Psi(k) dk \pmod{2\pi}, \quad (7)$$

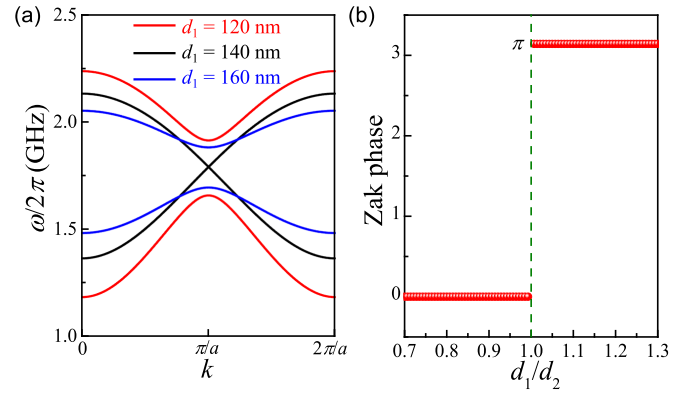


FIG. 3. (a) Band structure of an infinite DW racetrack for different intracellular lengths: $d_1 = 120, 140,$ and 160 nm, with d_2 being fixed to 140 nm. (b) Dependence of the Zak phase on the ratio d_1/d_2 .

where $\Psi(k)$ is the Bloch wave function of the energy band. Figure 3(b) shows the dependence of the Zak phase \mathbb{Z} on the ratio d_1/d_2 . It is observed that \mathbb{Z} is quantized to 0 when $d_1/d_2 < 1$ and to π otherwise, indicating two topologically distinct phases in the two regions. We point out that this conclusion is independent of the choice of d_2 .

Bulk-boundary correspondence indicates the existence of robust edge states. To verify this point, we compute the spectrum of a finite racetrack containing an odd number (e.g., 39) of DWs. Numerical results are shown in Fig. 4(a), where the in-gap state (red line) emerges for all ratios $d_1/d_2 \neq 1$. We first consider the case $d_1/d_2 = 8/7 (> 1)$. Figure 4(b) plots the eigenfrequencies of the system, showing that there is one in-gap mode marked by the red dot. Further, it is found that its spatial distribution is highly localized at the left end of the racetrack [see Fig. 4(c)], in contrast to its bulk counterpart shown in Fig. 4(d). We adopt the *Ansätze* for the localized mode as $q_j = q_j \exp(i\omega_0 t) z^n$ with $|z| < 1$. The edge state then can be solved by the equations

$$(I_1 + I_2 z)q_A(n) = 0, \text{ for } n = 1, 2, 3, \dots, \quad (8)$$

$$(I_1 + I_2 z^{-1})q_B(n) = 0, \text{ for } n = 2, 3, \dots,$$

with the boundary condition $I_1 q_B(1) = 0$ (A-site DW is in the outmost left boundary). Because $I_{1,2} \neq 0$, we obtain $q_B(n) = 0 \forall n$ and $z = -I_1/I_2$. The wave function of A-site DWs therefore follows an exponentially decaying formula $|q_A| = |q_0|(I_1/I_2)^n$ for $n = 1, 2, 3, \dots$. The analytical result agrees excellently with numerical calculations, as plotted in the inset of Fig. 4(c). We point out that the edge state becomes localized in the right end instead if $d_1/d_2 < 1$ (not shown). Interestingly, the localized modes emerge in both ends as the magnetic racetrack contains an even number of DWs (detailed calculations can be found in Appendix B).

To verify the topological robustness of the edge states, we calculate the spectrum of the DW racetrack including disorder and defects, with results presented in Figs. 4(e) and 4(f), respectively. Here the disorder is introduced by assuming that the coupling parameters I_1 and I_2 have a random variation, i.e., $I_1 \rightarrow I_1(1 + \delta N)$, $I_2 \rightarrow I_2(1 + \delta N)$, with δ the disorder strength and N a uniformly distributed random number between -1 and 1 . As to the defects, we assume I_1 and

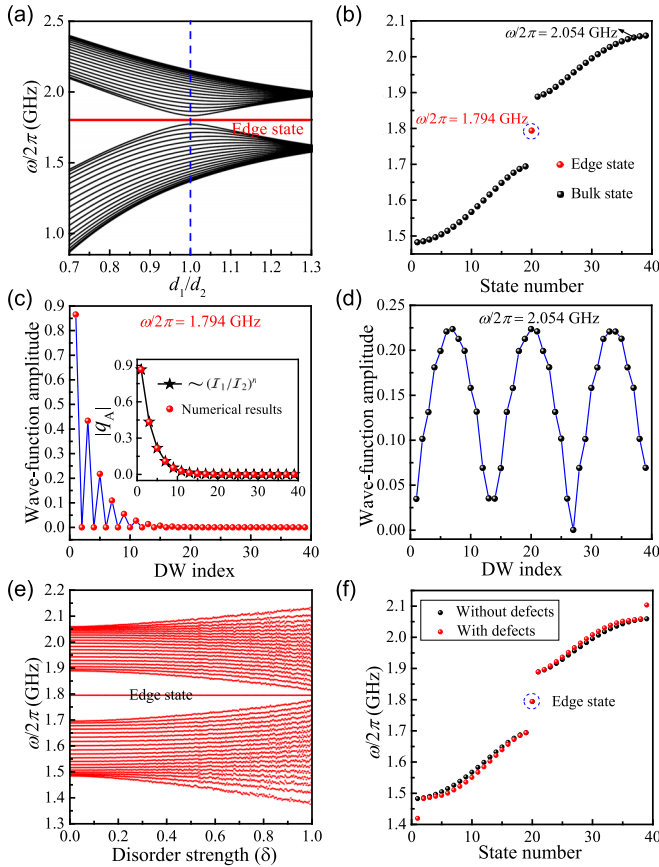


FIG. 4. (a) Spectrum of a finite DW racetrack for different d_1/d_2 . The dotted blue line denotes the boundary separating two topologically distinct phases; the red segment represents the in-gap mode. (b) Eigenfrequencies of the DW lattice with $d_1/d_2 = 8/7$. The spatial distribution of DW-oscillation amplitude for the edge (c) and bulk (d) states. Inset: Comparison between analytical and numerical results. (e) Spectrum of disordered DW racetracks. (f) Spectrum with (red dots) and without (black dots) defects.

I_2 suffering from a shift ($I_1 \rightarrow 10I_1$, $I_2 \rightarrow 0.1I_2$) on the second and fourth DWs. From Figs. 4(e) and 4(f), we observe that the edge state is very robust against the disorder and defects, while the bulk states are sensitive to them. It is worth noting that for the SSH model, the topological robustness of edge states is protected by the chiral symmetry. In other words, if the introduced disorder or defects respect the chiral symmetry, the edge states are still robust. The topological edge states become fragile if the disorder or defects break the chiral symmetry. In the above calculations, the disorder and defects are introduced into the off-diagonal elements of the Hamiltonian, which do respect the chiral symmetry, and the edge states are thus robust. However, if we consider disorder in the parameter \mathcal{K} , the chiral symmetry is broken and the edge states are no longer topologically protected (not shown).

B. Micromagnetic simulations

To confirm our theoretical predictions, we use the micromagnetic package MUMAX3 [68] to simulate the dynamics of 39 interacting DWs in a Ni nanostrip of length 7000 nm,

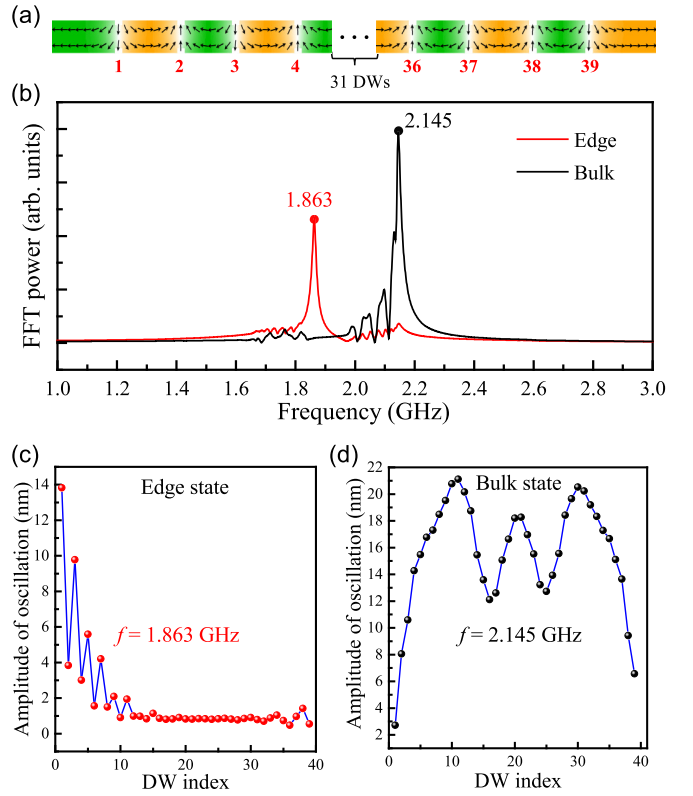


FIG. 5. (a) Schematic plot of a finite racetrack containing 39 DWs, with $d_1 = 160$ nm and $d_2 = 140$ nm. (b) The temporal Fourier spectra of the DW oscillations at edge (1st DW) and bulk (20th DW) positions. The spatial distribution of amplitude of DW oscillations for edge (c) and bulk (d) states.

as shown in Fig. 5(a). To obtain the spectra of DW oscillations, a sinc-function magnetic field $H(t) = H_0 \sin[2\pi f_0(t - t_0)]/[2\pi f_0(t - t_0)]$ is applied for $1 \mu\text{s}$ along the x axis with $H_0 = 10$ mT, $f_0 = 20$ GHz, and $t_0 = 1$ ns. The position of all DWs q_j is recorded every 100 ps, where we define $q_j = \int x |m_y|^2 dx / \int |m_y|^2 dx$ with the integration confined at the j th DW. Here, $|m_y|$ is adopted as the weight function based on the fact that the closer to the center of DW, the greater the y component of the magnetization.

To find the frequency range of the edge and bulk states, we analyze the temporal Fourier spectra of the DW racetrack at two different positions (DW 1 and DW 20, for example). Figure 5(b) shows the results, with peaks of the red and black curves denoting the positions of edge and bulk bands, respectively. We then apply a sinusoidal magnetic field $\mathbf{h}(t) = h_0 \sin(2\pi ft)\hat{x}$ with $h_0 = 0.05$ mT over the whole system to excite the edge and bulk modes by choosing two frequencies $f = 1.863$ and 2.145 GHz, respectively, as marked in Fig. 5(b). The spatial distributions of the DW-oscillation amplitudes for these two modes are plotted in Figs. 5(c) and 5(d), respectively, from which one can clearly identify the localized and extended nature of the edge and bulk states, respectively. Full micromagnetic simulations are thus well consistent with the analytical results but with the following discrepancies: (i) The oscillation of B-site DWs does not vanish as dictated by the analytical theory. We attribute it to the anharmonic DW-DW interaction between A-B sites (see Appendix C for

details). (ii) A finite DW oscillation is observed in the deep bulk of the racetrack, as opposed to an exponential decay to zero. However, we note that the amplitude in such case is smaller than the mesh size (2 nm) adopted in micromagnetic simulations. It is thus still within the numerical accuracy.

IV. DISCUSSION AND CONCLUSION

By including the STT term in Eq. (2), we find that it does not change the spectrum of the collective DW oscillations, but causes a global shift $X = \beta\gamma(N_y - N_z)M_s b_J/\omega_0^2$ to the equilibrium DW position (detailed analysis can be found in Appendix D). It is noted that the imaging of the DW position is already within current technology reach. Since the DW oscillation frequency ω_0 can be standardized by the topological method, we are able to accurately quantify the STT non-adiabaticity coefficient β by experimentally measuring the slope of the X - b_J curve.

It is worth mentioning that chapters 2 and 3 of Ref. [69] studied the edge states of a one-dimensional diatomic lattice of coupled masses. The wave function of edge modes with an exponential decay can be obtained by considering the boundary conditions. However, the topology of the diatomic lattice is not clear. Chen *et al.* investigate the 1D and 2D mechanical lattice by adopting the topological method [70]. They identify topological edge states by directly evaluating the Zak phase (the topological invariant) in a periodic spring-mass lattice without explicitly solving the boundary problem in the finite chain. The principle allowing doing so is the bulk-edge correspondence. Furthermore, from the state-of-the-art point of view, there are two different kinds of surface/edge states, namely, the topologically trivial and nontrivial surface/edge state. The former one is described by the Tamm-Shockley picture [71,72] which predicts that the periodicity breaking of the crystal potential at the boundary can lead to the formation of a conducting surface/edge state. However, this surface/edge state is trivial because it is sensitive to impurities, defects, and disorder. The latter one is described by a few topological invariants, such as the Chern number, Berry/Zak phase, etc. Because of the topological protection, it is quite robust against external disturbances. Sometimes, these two types of surface/edge modes exist simultaneously [73]. Without adopting the topological method, one can hardly distinguish them.

In summary, we studied the Su-Schrieffer-Heeger problem in a one-dimensional DW racetrack with periodic pinning notches. The Zak phase was evaluated to derive the phase diagram that allows two topologically distinct phases separated by the phase transition point at an identical intercellular and intracellular length between neighboring DWs. The emerging edge state dictated by the bulk-boundary correspondence was shown to be particularly robust against moderate defects and disorder. Analytical results were well supported by full micromagnetic simulations. We propose that the uncovered topological feature can be utilized as the DW frequency standard, which shall encourage our experimental colleagues to accurately measure the pinning profile and to finally resolve the controversy about the β parameter. For application, our model has some limitations and practical difficulties. On the one hand, the topologically stable edge states are protected by

the chiral symmetry, which indicates that these edge states are only immune from the disorder and defects to the coupling between domain walls but sensitive to them for the notch geometries. The superiority of our topological method thus depends on the technological level of notch fabrications in DW racetracks. On the other hand, the demagnetizing factors depends on the geometry of the system, the determination of which requires independent anisotropic ferromagnetic resonance measurements. Our general results are applicable to other types of solitons (e.g., magnetic vortex, skyrmion, bobber, meron, hopfion, etc). Our findings suggest as well that the magnetic soliton racetrack offers a unique playground to explore the fundamental topological phase, such as the topological corner (hinge) states in two- (three-) dimensional structures, and the nonlinear effect on topological phase transitions, which are interesting subjects for future study.

ACKNOWLEDGMENTS

This work was supported by the National Natural Science Foundation of China (NSFC) (Grants No. 12074057, No. 11604041, and No. 11704060) and the National Key Research Development Program under Contract No. 2016YFA0300801. Z.-X.L. acknowledges financial support from the China Postdoctoral Science Foundation (Grant No. 2019M663461) and the NSFC (Grant No. 11904048). Z.W. was supported by the China Postdoctoral Science Foundation under Grant No. 2019M653063.

APPENDIX A: THE DETERMINATION OF $\mathcal{I}(d)$

The d dependence of \mathcal{I} is the key for evaluating the band structures of the DW racetrack. To determine this function, we consider the dynamics of both a single DW and a DW-DW pair confined by notches in nanostrip, as shown in Figs. 6(a) and 6(b), respectively, where the distance between two DWs is set to be 144 nm. The following material parameters of Ni are used in the simulations [64]: the saturation magnetization $M_s = 0.477 \times 10^6$ A m⁻¹, exchange stiffness $A = 1.05 \times 10^{-11}$ J m⁻¹, and Gilbert damping constant $\alpha = 10^{-3}$. The length $L_x = 7000$ nm, width $L_y = 60$ nm, and thickness $L_z = 5$ nm. The cell size is $2 \times 3 \times 5$ nm³. We apply a sinc-function magnetic field $H(t) = H_0 \sin[2\pi f_0(t - t_0)]/[2\pi f_0(t - t_0)]$ along the x axis for 1 μ s with $H_0 = 10$ mT, $f_0 = 20$ GHz, and $t_0 = 1$ ns. This sinc function decays very fast with time. So, even with the amplitude H_0 is as high as 100 Oe, all physics is still in the linear region in the long run. Figures 6(c) and 6(d) plot the Fourier spectra of the oscillations for the single DW and the DW-DW pair, respectively. The frequencies of the peaks read $\omega_0/2\pi = 1.794$ GHz, $\omega_1/2\pi = 1.71$ GHz, and $\omega_2/2\pi = 2.033$ GHz. From Eq. (4) in the main text, we obtain the relations $\mathcal{K} = \mathcal{M}\omega_0^2$ and $\mathcal{I} = \mathcal{M}(\omega_2^2 - \omega_1^2)/2$. The effective mass of a single DW is evaluated as $\mathcal{M} = 2\mu_0 L_y L_z/\gamma^2(N_z - N_y)\Delta = 5.2097 \times 10^{-25}$ kg, where the demagnetizing factors $N_x = 0$, $N_y = 0.106$, and $N_z = 0.894$. Analytically, the demagnetizing factor can be calculated for a rectangular ferromagnetic prism once the geometry of the system is given [74]. Experimentally, the demagnetization factor can be measured by the ferromagnetic resonance spectrum along different directions of the device

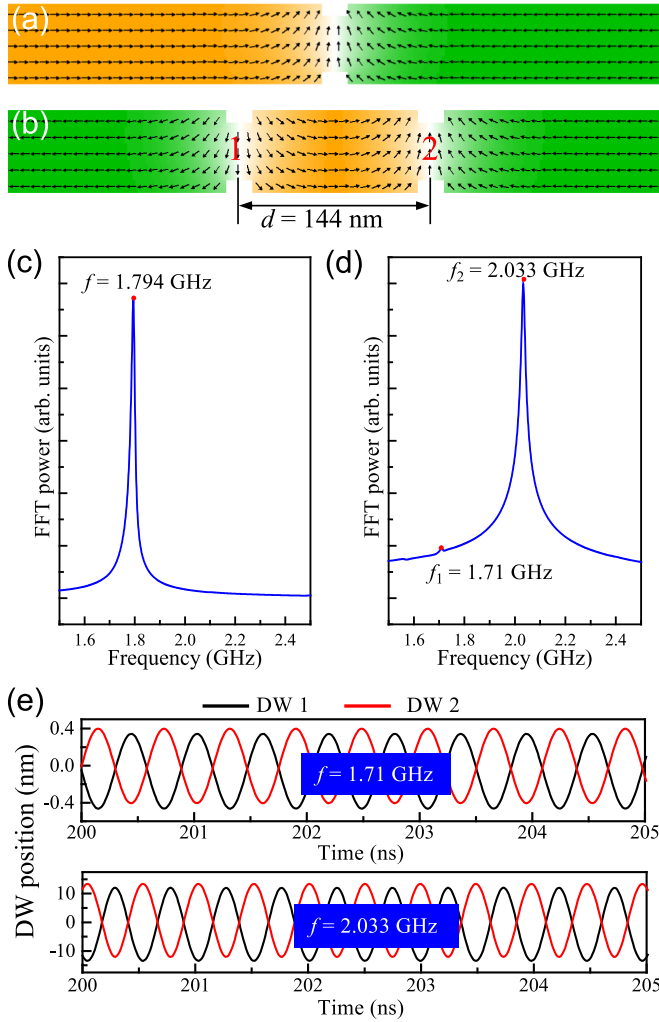


FIG. 6. Schematic plot of a single DW (a) and a DW-DW pair (b). The Fourier spectra of the DW oscillation for a single DW (c) and a DW-DW pair (d). (e) The DW position as a function of time for different modes.

[75,76]. Finally, we obtain $\mathcal{K} = 6.6194 \times 10^{-5} \text{ J m}^{-2}$ and $\mathcal{I} = 1.2433 \times 10^{-5} \text{ J m}^{-2}$ for $d = 144 \text{ nm}$. In these simulations, we did not consider any extrinsic disorder and defects, such that the obtained \mathcal{K} purely reflects the spring constant of the extrinsic pinning potential. By systematically varying the DW-DW distance, one can obtain the dependence of \mathcal{I} on d , as shown in Fig. 2(a) in the main text.

APPENDIX B: THE EDGE STATE CALCULATIONS FOR AN EVEN NUMBER OF DWs

In the main text, we have discussed the edge state of a finite racetrack with odd number of DWs, which shows that the in-gap state emerges for all ratios as long as $d_1/d_2 \neq 1$. These edge states are localized in the left or right end depending on the value of d_1/d_2 . Interestingly, when the system contains an even number (e.g., 40) of DWs [see Fig. 8(a)], the outcome is different and the localized modes appear in both ends. The band structure is shown in Fig. 7(a), from which one can see that the in-gap state can only exist when $d_1/d_2 > 1$.

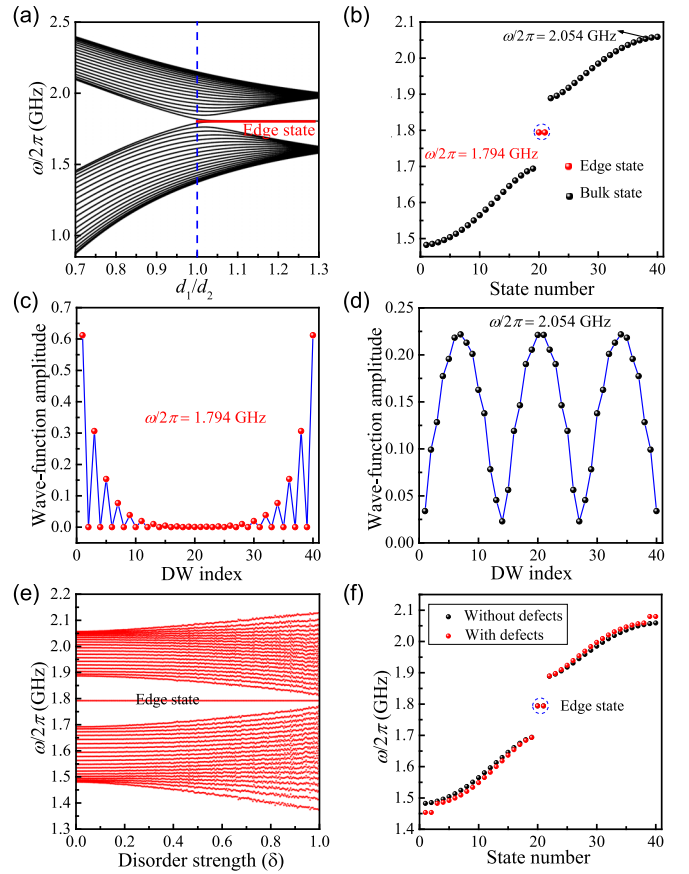


FIG. 7. (a) Spectrum of a finite racetrack containing 40 DWs for different d_1/d_2 . The red segment represents the in-gap mode. (b) Eigenfrequencies of the DW lattice with $d_1/d_2 = 8/7$. The spatial distribution of DW-oscillation amplitude for the edge (c) and bulk (d) states. (e) Spectrum of disordered DW racetracks. (f) Spectrum with (red dots) and without (black dots) defects.

In the following calculations, we consider $d_1/d_2 = 8/7$ as a representative example. Figure 7(b) plots the eigenfrequencies of the system, showing that there are two degenerate modes marked by the red balls. Further, we find that the spatial distribution of these degenerate modes is highly localized at both ends of the racetrack [see Fig. 7(c)], while the oscillation of bulk modes is spreading over the whole racetrack [see Fig. 7(d)]. In addition, we confirm as well that the edge states are very robust against disorder and defects, while the bulk states are not [see Figs. 7(e) and 7(f)].

Micromagnetic simulations are used to verify the theoretical predictions. The illustration of the system is shown in Fig. 8(a). By using the same method mentioned in the main text, we obtain the temporal Fourier spectra of the DW racetrack at the edge (DW 1) and bulk (DW 20) positions, as shown in Fig. 8(b). One can easily identify the edge and bulk modes. Furthermore, we choose two frequencies $f = 1.863$ and 2.144 GHz to show the oscillation characteristics of edge and bulk states, respectively. The spatial distributions of the DW-oscillation amplitudes with these two frequencies are plotted in Figs. 8(c) and 8(d). We observe the localized (at both ends) and extended nature for the edge and bulk states,

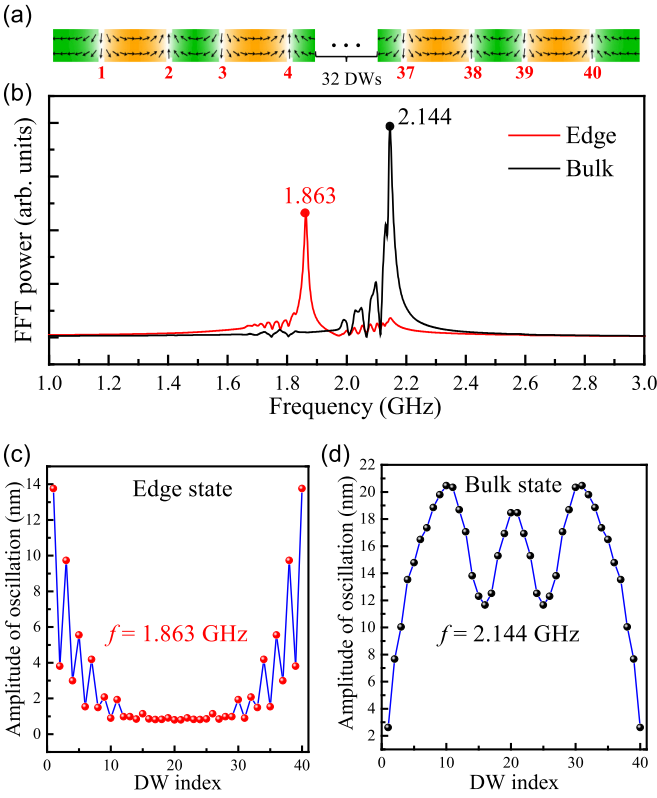


FIG. 8. (a) Schematic plot of a finite racetrack containing 40 DWs, with $d_1 = 160$ nm and $d_2 = 140$ nm. (b) The temporal Fourier spectra of the DW oscillation at edge (1st DW) and bulk (20th DW) positions. The spatial distribution of the DW oscillation amplitude for edge (c) and bulk (d) states.

respectively, which compares well with theoretical calculations [see Figs. 7(c) and 7(d)].

APPENDIX C: THE ANHARMONIC EFFECT

Next, we discuss the anharmonic effects in the two-DW system when the DW oscillation amplitude is large. We apply a sinusoidal magnetic field $\mathbf{h}(t) = h_0 \sin(2\pi ft)\hat{x}$ with $h_0 = 0.05$ mT and $f = 1.71$ GHz (and 2.033 GHz) to stimulate the dynamics of the DW-DW pair. In Fig. 6(e), we plot the displacement of DWs as a function of time. Surprisingly, we observe that both modes are out of phase, and the oscillation amplitude of mode 1 is one order of magnitude smaller than that of mode 2. This result is in sharp contrast to that in the

linearly coupled DW-DW pair:

$$\begin{aligned} \mathcal{M} \frac{d^2 q_1}{dt^2} + \mathcal{K} q_1 + \mathcal{I} q_2 &= 0, \\ \mathcal{M} \frac{d^2 q_2}{dt^2} + \mathcal{K} q_2 + \mathcal{I} q_1 &= 0, \end{aligned} \quad (\text{C1})$$

from which we obtain two eigenfrequencies $\omega_{1,2} = \sqrt{(\mathcal{K} \mp \mathcal{I})/\mathcal{M}}$ with corresponding eigenfunctions $q_1 = -q_2$ and $q_1 = q_2$, respectively. The former solution represents the out-of-phase mode, while the latter one corresponds to the in-phase mode. To interpret the discrepancy between the numerical result and theoretical calculation, we introduce a nonlinear term $\frac{\varepsilon q_1^2 q_2^2}{2}$ to the DW-DW coupling, where $\varepsilon > 0$ represents the nonlinearity strength. We then obtain the nonlinearly coupled equations of motion for the DW-DW pair:

$$\begin{aligned} \mathcal{M} \frac{d^2 q_1}{dt^2} + (\mathcal{K} + \varepsilon q_2^2) q_1 + \mathcal{I} q_2 &= 0, \\ \mathcal{M} \frac{d^2 q_2}{dt^2} + (\mathcal{K} + \varepsilon q_1^2) q_2 + \mathcal{I} q_1 &= 0. \end{aligned} \quad (\text{C2})$$

In line with micromagnetic simulations, we impose the DW-DW pair to support the out-of-phase modes only, i.e., $q_1 = -q_2 = q$. Equations (C2) then can be simplified to

$$\mathcal{M} \frac{d^2 q}{dt^2} + (\mathcal{K} + \varepsilon |q|^2) q - \mathcal{I} q = 0. \quad (\text{C3})$$

The presence of the nonlinear coupling will cause a frequency shift: $\omega_1 \rightarrow \Omega_1 = \sqrt{(\mathcal{K} - \mathcal{I} + \delta_1)/\mathcal{M}}$ and $\omega_2 \rightarrow \Omega_2 = \sqrt{(\mathcal{K} + \mathcal{I} + \delta_2)/\mathcal{M}}$. Substituting Ω_1 and Ω_2 into Eq. (C3), we obtain $\delta_1 = \varepsilon |q|^2$ and $\delta_2 = \varepsilon |q|^2 - 2\mathcal{I}$. It can be clearly seen that δ_1 (δ_2) approaches zero only if $|q| \rightarrow 0$ ($|q| \rightarrow \sqrt{2\mathcal{I}/\varepsilon}$) for a given ε , which is consistent with the numerical findings that the oscillation amplitude of the ω_2 mode is much higher than that of the ω_1 mode and both modes are out of phase [see Fig. 6(e)]. We thus conclude that the anharmonic coupling between DWs leads to two out-of-phase modes, which well explains the results observed in micromagnetic simulations.

APPENDIX D: THE STT EFFECT ON THE DW MOTION

The STT effect can be included in the generalized Landau-Lifshitz-Gilbert equation:

$$\begin{aligned} (1 + \alpha^2) \frac{dq}{dt} &= \gamma \alpha H_{\text{pin}} \Delta + \frac{1}{2} \gamma (N_z - N_y) \Delta M_s \sin 2\phi - (1 + \alpha \beta) b_J, \\ (1 + \alpha^2) \frac{d\phi}{dt} &= \gamma H_{\text{pin}} - \frac{1}{2} \gamma \alpha (N_z - N_y) M_s \sin 2\phi + \frac{b_J}{\Delta} (\alpha - \beta). \end{aligned} \quad (\text{D1})$$

For theoretical simplicity, we consider the dynamics of a single DW, such that the subscript j was removed in the above equations. By linearizing Eq. (D1) and neglecting the

dissipation terms, we obtain

$$\frac{d^2 q}{dt^2} + \frac{\mathcal{K}}{\mathcal{M}} q = -\beta \gamma (N_z - N_y) M_s b_J. \quad (\text{D2})$$

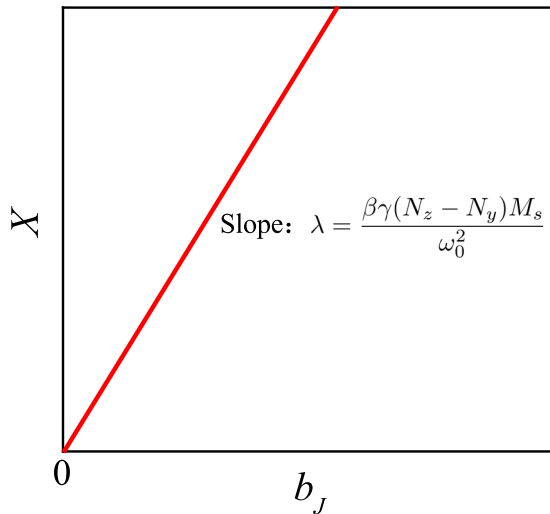


FIG. 9. Proposed scheme to determine the STT non-adiabaticity β by experimentally measuring the slope of X - b_J curve.

The solution of (D2) can be written as

$$q(t) = q_0 \exp(i\omega_0 t) - \frac{\beta\gamma(N_z - N_y)M_s b_J}{\omega_0^2}. \quad (\text{D3})$$

From Eq. (D3), we find that the STT does not modify the DW-oscillation frequency but causes a shift to its equilibrium position:

$$X = |\langle q(t) \rangle| = \frac{\beta\gamma(N_z - N_y)M_s b_J}{\omega_0^2}. \quad (\text{D4})$$

The non-adiabaticity parameter β can therefore be accurately quantified by experimentally measuring the slope of the X - b_J curve, i.e., $\lambda = \beta\gamma(N_z - N_y)M_s/\omega_0^2$. The proposal is schematically illustrated in Fig. 9. For the typical parameters $\beta = 0.01$, $J = 3 \times 10^{12}$ A/m², and $P = 0.7$, we can estimate the size of the average displacement $|\langle q(t) \rangle| \approx 10.5$ nm.

- [1] A. Wachowiak, J. Wiebe, M. Bode, O. Pietzsch, M. Morgenstern, and R. Wiesendanger, Direct observation of internal spin structure of magnetic vortex cores, *Science* **298**, 577 (2002).
- [2] B. Van Waeyenberge, A. Puzic, H. Stoll, K. W. Chou, T. Tylizszczak, R. Hertel, M. Fähnle, H. Brückl, K. Rott, G. Reiss, I. Neudecker, D. Weiss, C. H. Back, and G. Schütz, Magnetic vortex core reversal by excitation with short bursts of an alternating field, *Nature (London)* **444**, 461 (2006).
- [3] I. Makhfudz, B. Krüger, and O. Tchernyshyov, Inertia and Chiral Edge Modes of a Skyrmion Magnetic Bubble, *Phys. Rev. Lett.* **109**, 217201 (2012).
- [4] K.-W. Moon, B. S. Chun, W. Kim, Z. Q. Qiu, and C. Hwang, Control of skyrmion magnetic bubble gyration, *Phys. Rev. B* **89**, 064413 (2014).
- [5] S. Mühlbauer, B. Binz, F. Jonietz, C. Pfleiderer, A. Rosch, A. Neubauer, R. Georgii, and P. Böni, Skyrmion lattice in a chiral magnet, *Science* **323**, 915 (2009).
- [6] W. Jiang, P. Upadhyaya, W. Zhang, G. Yu, M. B. Jungfleisch, F. Y. Fradin, J. E. Pearson, Y. Tserkovnyak, K. L. Wang, O. Heinonen, S. G. E. te Velthuis, and A. Hoffmann, Blowing magnetic skyrmion bubbles, *Science* **349**, 283 (2015).
- [7] D. Atkinson, D. A. Allwood, G. Xiong, M. D. Cooke, C. C. Faulkner, and R. P. Cowburn, Magnetic domain-wall dynamics in a submicrometre ferromagnetic structure, *Nat. Mater.* **2**, 85 (2003).
- [8] G. Catalan, J. Seidel, R. Ramesh, and J. F. Scott, Domain wall nanoelectronics, *Rev. Mod. Phys.* **84**, 119 (2012).
- [9] T. Koyama, D. Chiba, K. Ueda, K. Kondou, H. Tanigawa, S. Fukami, T. Suzuki, N. Ohshima, N. Ishiwata, Y. Nakatani, K. Kobayashi, and T. Ono, Observation of the intrinsic pinning of a magnetic domain wall in a ferromagnetic nanowire, *Nat. Mater.* **10**, 194 (2011).
- [10] F. Jonietz, S. Mühlbauer, C. Pfleiderer, A. Neubauer, W. Münzer, A. Bauer, T. Adams, R. Georgii, P. Böni, R. A. Duine, K. Everschor, M. Garst, and A. Rosch, Spin transfer torques in MnSi at ultralow current densities, *Science* **330**, 1648 (2010).
- [11] X. Z. Yu, N. Kanazawa, W. Z. Zhang, T. Nagai, T. Hara, K. Kimoto, Y. Matsui, Y. Onose, and Y. Tokura, Skyrmion flow near room temperature in an ultralow current density, *Nat. Commun.* **3**, 988 (2012).
- [12] V. S. Pribiag, I. N. Krivorotov, G. D. Fuchs, P. M. Braganca, O. Ozatay, J. C. Sankey, D. C. Ralph, and R. A. Buhrman, Magnetic vortex oscillator driven by d.c. spin-polarized current, *Nat. Phys.* **3**, 498 (2007).
- [13] S. Zhang, J. Wang, Q. Zheng, Q. Zhu, X. Liu, S. Chen, C. Jin, Q. Liu, C. Jia, and D. Xue, Current-induced magnetic skyrmions oscillator, *New J. Phys.* **17**, 023061 (2015).
- [14] A. Fert, V. Cros, and J. Sampaio, Skyrmions on the track, *Nat. Nanotechnol.* **8**, 152 (2013).
- [15] D. A. Allwood, G. Xiong, C. C. Faulkner, D. Atkinson, D. Petit, and R. P. Cowburn, Magnetic domain-wall logic, *Science* **309**, 1688 (2005).
- [16] P. Xu, K. Xia, C. Gu, L. Tang, H. Yang, and J. Li, An all-metallic logic gate based on current-driven domain wall motion, *Nat. Nanotechnol.* **3**, 97 (2008).
- [17] K. A. Omari and T. J. Hayward, Chirality-Based Vortex Domain-Wall Logic Gates, *Phys. Rev. Appl.* **2**, 044001 (2014).
- [18] Z. Luo, A. Hrabec, T. P. Dao, G. Sala, S. Finizio, J. Feng, S. Mayr, J. Raabe, P. Gambardella, and L. J. Heyderman, Current-driven magnetic domain-wall logic, *Nature (London)* **579**, 214 (2020).
- [19] T. Ono and Y. Nakatani, Magnetic domain wall oscillator, *Appl. Phys. Express* **1**, 061301 (2008).
- [20] J. He and S. Zhang, Localized steady-state domain wall oscillators, *Appl. Phys. Lett.* **90**, 142508 (2007).
- [21] E. Martinez, L. Torres, and L. Lopez-Diaz, Oscillator based on pinned domain walls driven by direct current, *Phys. Rev. B* **83**, 174444 (2011).
- [22] S. S. P. Parkin, M. Hayashi, and L. Thomas, Magnetic domain-wall racetrack memory, *Science* **320**, 190 (2008).
- [23] S. Parkin and S.-H. Yang, Memory on the racetrack, *Nat. Nanotechnol.* **10**, 195 (2015).

- [24] B. Borie, A. Kehlberger, J. Wahrhusen, H. Grimm, and M. Kläui, Geometrical Dependence of Domain-Wall Propagation and Nucleation Fields in Magnetic-Domain-Wall Sensors, *Phys. Rev. Appl.* **8**, 024017 (2017).
- [25] M. Hayashi, L. Thomas, C. Rettner, R. Moriya, X. Jiang, and S. S. P. Parkin, Dependence of Current and Field Driven Depinning of Domain Walls on Their Structure and Chirality in Permalloy Nanowires, *Phys. Rev. Lett.* **97**, 207205 (2006).
- [26] S. Lepadatu, A. Vanhaverbeke, D. Atkinson, R. Allenspach, and C. H. Marrows, Dependence of Domain-Wall Depinning Threshold Current on Pinning Profile, *Phys. Rev. Lett.* **102**, 127203 (2009).
- [27] H. T. Fook, W. L. Gan, and W. S. Lew, Gateable skyrmion transport via field-induced potential barrier modulation, *Sci. Rep.* **6**, 21099 (2016).
- [28] L. D. Geng and Y. M. Jin, Magnetic vortex racetrack memory, *J. Magn. Magn. Mater.* **423**, 84 (2017).
- [29] H. Y. Yuan and X. R. Wang, Domain wall pinning in notched nanowires, *Phys. Rev. B* **89**, 054423 (2014).
- [30] D. Bedau, M. Kläui, M. T. Hua, S. Krzyk, U. Rüdiger, G. Faini, and L. Vila, Quantitative Determination of the Nonlinear Pinning Potential for a Magnetic Domain Wall, *Phys. Rev. Lett.* **101**, 256602 (2008).
- [31] H. T. Zeng, D. Read, D. Petit, A. V. Jausovec, L. O'Brien, E. R. Lewis, and R. P. Cowburn, Combined electrical and magneto-optical measurements of the magnetization reversal process at a domain wall trap, *Appl. Phys. Lett.* **94**, 103113 (2009).
- [32] E. R. Lewis, D. Petit, L. O'Brien, A.-V. Jausovec, H. T. Zeng, D. E. Read, and R. P. Cowburn, Kinetic depinning of a magnetic domain wall above the Walker field, *Appl. Phys. Lett.* **98**, 042502 (2011).
- [33] L. J. Chang, P. Lin, and S. F. Lee, Current induced localized domain wall oscillators in NiFe/Cu/NiFe submicron wires, *Appl. Phys. Lett.* **101**, 242404 (2012).
- [34] M. Franchin, A. Knittel, M. Albert, D. S. Chernyshenko, T. Fischbacher, A. Prabhakar, and H. Fangohr, Enhanced spin transfer torque effect for transverse domain walls in cylindrical nanowires, *Phys. Rev. B* **84**, 094409 (2011).
- [35] D. Petit, A.-V. Jausovec, D. Read, and R. P. Cowburn, Domain wall pinning and potential landscapes created by constrictions and protrusions in ferromagnetic nanowires, *J. Appl. Phys.* **103**, 114307 (2008).
- [36] S. Glathe and R. Mattheis, Magnetic domain wall pinning by kinks in magnetic nanostripes, *Phys. Rev. B* **85**, 024405 (2012).
- [37] J. Akerman, M. Muñoz, M. Maicas, and J. L. Prieto, Stochastic nature of the domain wall depinning in permalloy magnetic nanowires, *Phys. Rev. B* **82**, 064426 (2010).
- [38] J. He, Z. Li, and S. Zhang, Current-driven domain-wall depinning, *J. Appl. Phys.* **98**, 016108 (2005).
- [39] D. Ravelosona, D. Lacour, J. A. Katine, B. D. Terris, and C. Chappert, Nanometer Scale Observation of High Efficiency Thermally Assisted Current-Driven Domain Wall Depinning, *Phys. Rev. Lett.* **95**, 117203 (2005).
- [40] S. Lepadatu, M. C. Hickey, A. Potenza, H. Marchetto, T. R. Charlton, S. Langridge, S. S. Dhesi, and C. H. Marrows, Experimental determination of spin-transfer torque nonadiabaticity parameter and spin polarization in permalloy, *Phys. Rev. B* **79**, 094402 (2009).
- [41] S. Lepadatu, J. S. Claydon, C. J. Kinane, T. R. Charlton, S. Langridge, A. Potenza, S. S. Dhesi, P. S. Keatley, R. J. Hicken, B. J. Hickey, and C. H. Marrows, Domain-wall pinning, nonadiabatic spin-transfer torque, and spin-current polarization in permalloy wires doped with vanadium, *Phys. Rev. B* **81**, 020413(R) (2010).
- [42] G. Meier, M. Bolte, R. Eiselt, B. Krüger, D. Kim, and P. Fischer, Direct Imaging of Stochastic Domain-Wall Motion Driven by Nanosecond Current Pulses, *Phys. Rev. Lett.* **98**, 187202 (2007).
- [43] R. Moriya, L. Thomas, M. Hayashi, Y. B. Bazaliy, C. Rettner, and S. S. P. Parkin, Probing vortex-core dynamics using current-induced resonant excitation of a trapped domain wall, *Nat. Phys.* **4**, 368 (2008).
- [44] L. Heyne, J. Rhensius, D. Ilgaz, A. Bisig, U. Rüdiger, M. Kläui, L. Joly, F. Nolting, L. J. Heyderman, J. U. Thiele, and F. Kronast, Direct Determination of Large Spin-Torque Nonadiabaticity in Vortex Core Dynamics, *Phys. Rev. Lett.* **105**, 187203 (2010).
- [45] L. Thomas, M. Hayashi, X. Jiang, R. Moriya, C. Rettner, and S. S. P. Parkin, Oscillatory dependence of current-driven magnetic domain wall motion on current pulse length, *Nature (London)* **443**, 197 (2006).
- [46] A. Bisig, C. A. Akosa, J.-H. Moon, J. Rhensius, C. Moutafis, A. von Bieren, J. Heidler, G. Kiliani, M. Kammerer, M. Curcic, M. Weigand, T. Tyliczszak, B. Van Waeyenberge, H. Stoll, G. Schütz, K.-J. Lee, A. Manchon, and M. Kläui, Enhanced Nonadiabaticity in Vortex Cores due to the Emergent Hall Effect, *Phys. Rev. Lett.* **117**, 277203 (2016).
- [47] W. Jiang, Y. Fan, P. Upadhyaya, M. Lang, M. Wang, L.-T. Chang, K. L. Wong, J. Tang, M. Lewis, J. Zhao, L. He, X. Kou, C. Zeng, X. Z. Zhou, R. N. Schwartz, and K. L. Wang, Mapping the domain wall pinning profile by stochastic imaging reconstruction, *Phys. Rev. B* **87**, 014427 (2013).
- [48] R. Badae and J. Berezovsky, Mapping the Landscape of Domain-Wall Pinning in Ferromagnetic Films Using Differential Magneto-Optical Microscopy, *Phys. Rev. Appl.* **5**, 064003 (2016).
- [49] K. v. Klitzing, G. Dorda, and M. Pepper, New Method for High-Accuracy Determination of the Fine-Structure Constant Based on Quantized Hall Resistance, *Phys. Rev. Lett.* **45**, 494 (1980).
- [50] R. Shindou, J.-i. Ohe, R. Matsumoto, S. Murakami, and E. Saitoh, Chiral spin-wave edge modes in dipolar magnetic thin films, *Phys. Rev. B* **87**, 174402 (2013).
- [51] R. Shindou, R. Matsumoto, S. Murakami, and J.-i. Ohe, Topological chiral magnonic edge mode in a magnonic crystal, *Phys. Rev. B* **87**, 174427 (2013).
- [52] A. Mook, J. Henk, and I. Mertig, Edge states in topological magnon insulators, *Phys. Rev. B* **90**, 024412 (2014).
- [53] R. Chisnell, J. S. Helton, D. E. Freedman, D. K. Singh, R. I. Bewley, D. G. Nocera, and Y. S. Lee, Topological Magnon Bands in a Kagome Lattice Ferromagnet, *Phys. Rev. Lett.* **115**, 147201 (2015).
- [54] X. S. Wang, Y. Su, and X. R. Wang, Topologically protected unidirectional edge spin waves and beam splitter, *Phys. Rev. B* **95**, 014435 (2017).
- [55] S. K. Kim and Y. Tserkovnyak, Chiral Edge Mode in the Coupled Dynamics of Magnetic Solitons in a Honeycomb Lattice, *Phys. Rev. Lett.* **119**, 077204 (2017).

- [56] G. Go, I.-S. Hong, S.-W. Lee, S. K. Kim, and K.-J. Lee, Realization of Su-Schrieffer-Heeger states based on metamaterials of magnetic solitons, *Phys. Rev. B* **101**, 134423 (2020).
- [57] Z.-X. Li, Y. Cao, P. Yan, and X. R. Wang, Higher-order topological solitonic insulators, *npj Comput. Mater.* **5**, 107 (2019).
- [58] Z.-X. Li, Y. Cao, X. R. Wang, and P. Yan, Symmetry-Protected Zero Modes in Metamaterials Based on Topological Spin Texture, *Phys. Rev. Appl.* **13**, 064058 (2020).
- [59] Z.-X. Li, Y. Cao, X. R. Wang, and P. Yan, Second-order topological solitonic insulator in a breathing square lattice of magnetic vortices, *Phys. Rev. B* **101**, 184404 (2020).
- [60] S. Zhang and Z. Li, Roles of Nonequilibrium Conduction Electrons on the Magnetization Dynamics of Ferromagnets, *Phys. Rev. Lett.* **93**, 127204 (2004).
- [61] A. Thiaville, Y. Nakatani, J. Miltat, and Y. Suzuki, Micromagnetic understanding of current-driven domain wall motion in patterned nanowires, *Europhys. Lett.* **69**, 990 (2005).
- [62] N. L. Schryer and L. R. Walker, The motion of 180° domain walls in uniform dc magnetic fields, *J. Appl. Phys.* **45**, 5406 (1974).
- [63] Z. Li and S. Zhang, Domain-wall dynamics driven by adiabatic spin-transfer torques, *Phys. Rev. B* **70**, 024417 (2004).
- [64] A. Pivano and V. O. Dolocan, Analytical description of the topological interaction between magnetic domain walls in nanowires, *Phys. Rev. B* **101**, 014438 (2020).
- [65] W. P. Su, J. R. Schrieffer, and A. J. Heeger, Solitons in Polyacetylene, *Phys. Rev. Lett.* **42**, 1698 (1979).
- [66] F. Schindler, Dirac equation perspective on higher-order topological insulators, *J. Appl. Phys.* **128**, 221102 (2020).
- [67] J. Zak, Berry's Phase for Energy Bands in Solids, *Phys. Rev. Lett.* **62**, 2747 (1989).
- [68] A. Vansteenkiste, J. Leliaert, M. Dvornik, M. Helsen, F. Garcia-Sanchez, and B. V. Waeyenberge, The design and verification of MuMax3, *AIP Adv.* **4**, 107133 (2014).
- [69] M. G. Cottam and D. R. Tilley, *Introduction to Surface and Superlattice Excitations* (Cambridge University Press, Cambridge, UK, 2005).
- [70] H. Chen, H. Nassar, and G. L. Huang, A study of topological effects in 1D and 2D mechanical lattices, *J. Mech. Phys. Solids* **117**, 22 (2018).
- [71] I. Tamm, Über eine mögliche Art der Elektronenbindung an Kristalloberflächen, *Phys. Z. Sowjetunion* **76**, 849 (1932).
- [72] W. Shockley, On the surface states associated with a periodic potential, *Phys. Rev.* **56**, 317 (1939).
- [73] Z.-X. Li, C. Wang, Y. Cao, and P. Yan, Edge states in a two-dimensional honeycomb lattice of massive magnetic skyrmions, *Phys. Rev. B* **98**, 180407(R) (2018).
- [74] A. Aharoni, Demagnetizing factors for rectangular ferromagnetic prisms, *J. Appl. Phys.* **83**, 3432 (1998).
- [75] O. Kohmoto, Effective demagnetizing factors in ferromagnetic resonance equations, *J. Magn. Magn. Mater.* **262**, 280 (2003).
- [76] K. S. Muster and R. Heindl, Determination of demagnetizing factors using first-order reversal curves and ferromagnetic resonance, *AIP Adv.* **10**, 015318 (2020).